42nd AIAA Plasmadynamics and Lasers Conference
 in conjunction with the
 18th Internati
27 - 30 June 2011, Honolulu, Hawaii
AIAA 2011-3276

Identification, Prediction and Control of Aero Optical Wavefronts in Laser Beam Propagation

Jonathan Tesch and Steve Gibson
Mechanical and Aerospace Engineering, University of California, Los Angeles 90095-1597

Stanislav Gordeyev and Eric Jumper
Aerospace and Mechanical Engineering, University of Notre Dame, Notre Dame, IN 46556-5637

This paper describes linear time-invariant optimal prediction and control of aero-optical wavefronts derived from recent flight-test data. The optimal controller is based on an optimal prediction filter that has the form of a multi-input-multi-output state-space model that captures the statistics of the aero-optical wavefront sequence. Experimental result in the paper show the improvement in wavefront correction achieved by an optimal controller based on the identified prediction filter, as opposed to a classical adaptive optics loop.

I. Introduction

In recent research on adaptive optics, improved wavefront correction has been achieved through wavefront prediction by both adaptive filtering an control[1–6] and by optimal linear time-invariant (LTI) filtering and control.[9–11] For stationary or quasi-stationary turbulence, optimal LTI controllers are potentially as effective as fully adaptive controller, while being less complex and less black-box than fully adaptive controllers. As with adaptive controllers that have been used for adaptive optics (AO), optimal LTI controllers predict wavefront sequences to mitigate loop latency and the limited bandwidth of classical AO loops. Without a prediction capability, the only way to improve the bandwidth of wavefront correction is to increase the frame rate of the AO loop.

This paper describes an optimal (i.e., minimum-variance) LTI controller based on a wavefront-prediction filter identified from measured wavefront data. The control and system identification methods are demonstrated by results from an adaptive optics experiment in which the disturbance wavefront sequence is derived from wavefront data obtained in recent flight tests that measured aero-optical effects on a laser beam propagating between two airplanes. The optimal prediction filters have the form of multi-input-multi-output state space models that capture the statistics of the aero-optical wavefront sequences.

The prediction filter in this paper has the form of Kalman predictors, but it is not obtained by the standard methods of Kalman filter/predictor design, where known or assumed plant models along with disturbance and noise statistics are used to design a Kalman filter. Rather, the prediction filters are identified directly from measured wavefront data sequences by a subspace system identification method, with no required *a priori* knowledge of the turbulence statistics. A related approach to adaptive optics has been demonstrated in [10], although several aspects of the controller design and system identification are different here, including the integration of optimal control with a classical AO loop, the frequency-weighted deformable mirror modes used here to reduce the number of control channels, and the lattice-filter based subspace system identification algorithm.

II. Description of the Experiment

The main components of the experiment are a laser source, two deformable mirrors, a Shack-Hartmann wavefront sensor and a target camera (i.e., scoring camera). Figure 1 shows a photograph of the experiment, and Figure 2 shows a corresponding diagram.

The control actuator is the deformable mirror denoted by DM1 in Figure 2, which is a 31-actuator one-inch membrane mirror from Active Optical Systems (AOS). The deformable mirror denoted by DM2 adds the aero-optical wavefronts to the beam; DM2 is a 61-actuator one-inch membrane mirror from AOS. The Shack-Hartmann sensor measures the wavefront on a 10×10 subaperture array. A PC running MATLAB reads the Shack-Hartmann and target-camera images, converts the Shack-Hartmann images to wavefront slope vectors, computes the control commands and sends them to DM1.

The experiment runs at a frame rate of approximately 30 Hz due to hardware limitations. However, the original aero-optical flight-test data was sampled at a 16 KHz frame rate, which determines the temporal statistics of the wavefront sequence used in the experiment reported here.

III. Commands to the DMs

A. Control Commands

The deformable mirror DM1 is identical to the DM used in [6] for adaptive control in adaptive optics. The actuator command voltages v_i generate electric fields that produce DM displacements (i.e., phase shifts) d_i at the individual actuators, with displacements and commands related by

$$d_i = a v_i^2 \tag{1}$$

where a is a constant. The electronic driver for the deformable mirror provides eight-bit resolution for the DM commands taking integer values between 0 and 255. For the control loops, the command voltages are parameterized as

$$v_i = \text{round}\left(\sqrt{c_i + v_\text{b}^2}\right), \qquad v_\text{b} = 180 \simeq \sqrt{255^2/2} \tag{2}$$

where c_i is a control command and v_b is an applied bias voltage. The bias voltage v_b, which is the same for all actuators, produces a focus shape on the DM. The commands c_i can take values in the interval $-v_\text{b}^2 \le c_i \le v_\text{b}^2$. If the quantization error due to the rounding is neglected, then (1) and (2) yield

$$d_i = a(c_i + v_\text{b}^2). \tag{3}$$

B. Disturbance Commands

The deformable mirror DM2 is similar to DM1 but with 61 actuators instead of the 31 actuators for DM1. The relationship among the command voltages, disturbance commands and displacements of DM2 are parameterized as in (1)–(3), with the vector of disturbance commands for DM2 denoted by c_w.

To determine the disturbance commands for DM2, a sequence of wavefronts measured in the Notre Dame airborne aero-optics laboratory[7] were mapped to the geometry of DM2. Of course, the original wavefronts had higher resolution than the 61 degrees of freedom provided by DM2, but the dominant wavefront statistics were preserved. The measured aero-optical wavefronts also had a central hole due to a common obscuration in the optical system. Before mapping the wavefronts to the DM2 geometry, the hole was filled by a multichannel prediction filter that used both spatial and temporal information from the measured pixels to estimate the values of missing pixels. The filter gains were determined by least-squares estimation of a prediction model for the measured pixels.

IV. Adaptive Optics and Optimal Control

A. The Adaptive Optics Problem

The block diagram in Figure 3 shows the signals and control loops for the adaptive optics problem. For control design, the following model represents the part of the block diagram between c and y:

$$y = y_\text{b} + w - \Gamma c\,. \tag{4}$$

Here Γ is the poke matrix, which was by least-squares estimation with input/output data from a preliminary experiment in which DM1 was driven open-loop with a broadband command sequence.

The classical adaptive optics (AO) loop shown in Figure 3 consists of a low-pass digital filter with gain $K = 0.5$ and pole $\alpha = 0.98$, the modal transformation matrix U and the least-squares reconstructor E. The

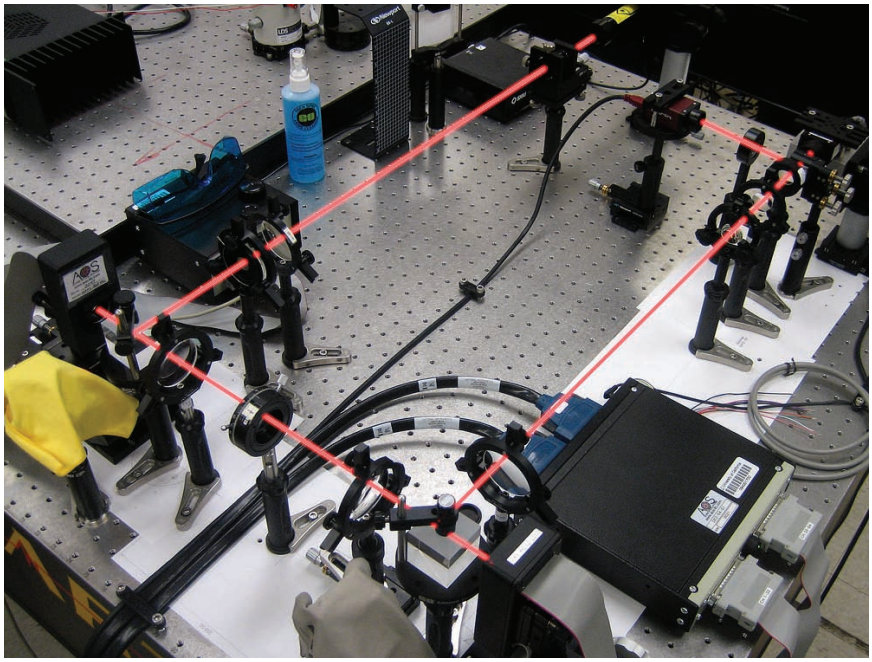

Figure 1. Photograph of the experiment.

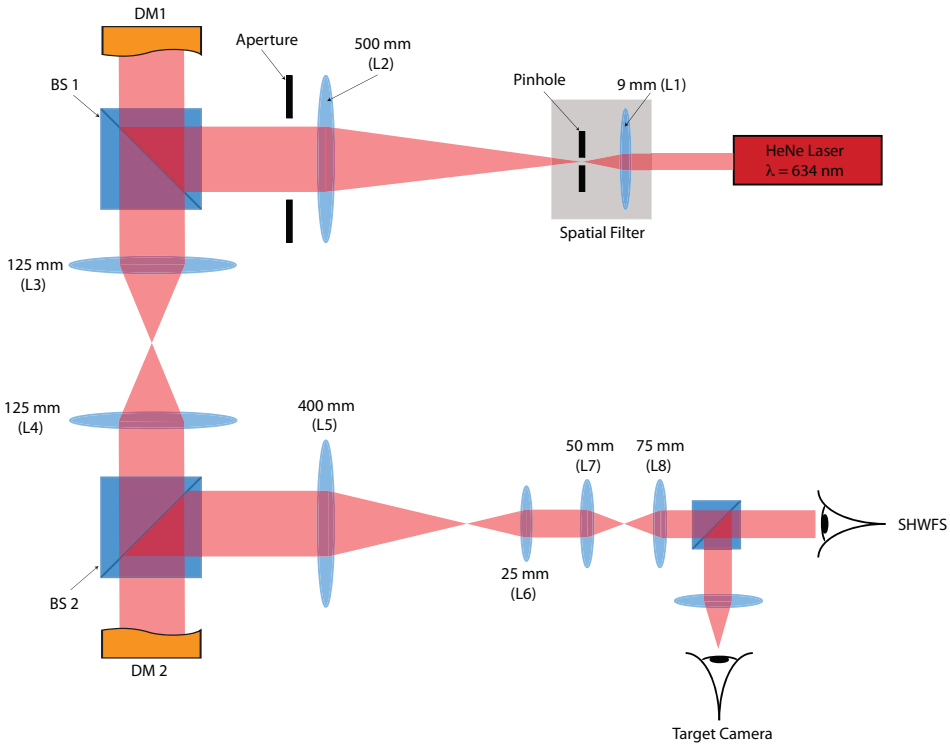

Figure 2. Diagram of the experiment.

low-pass filter, which is an integrator when $\alpha = 1$, is a diagonal multi-input-multi-output (MIMO) filter with each diagonal element equal to the same scalar transfer function. The values of K and α were chosen through experimental trial and error with the Turbulence 1 wavefront disturbance to maximize the error-rejection bandwidth of the classical AO loop without amplifying high-frequency disturbance and noise. The z^{-1} block in Figure 3 indicates that the AO system has a one-frame loop latency.

The columns of U represent a set of frequency-weighted deformable mirror (DM) modes that are orthogonal with respect to the actuator influence functions. These modes are discussed in detail in [6]. The mode images (i.e.; DM surface shapes) are shown in Figure 4. Both the classical AO loop and the optimal control loop use the DM modes as control channels. The reconstructor matrix E is the pseudo inverse of ΓU. Since the poke matrix Γ has linearly independent columns,

$$E \Gamma U = I, \tag{5}$$

which implies that the modal control channels are uncoupled in the linear model of the system when only the classical AO loop is closed.

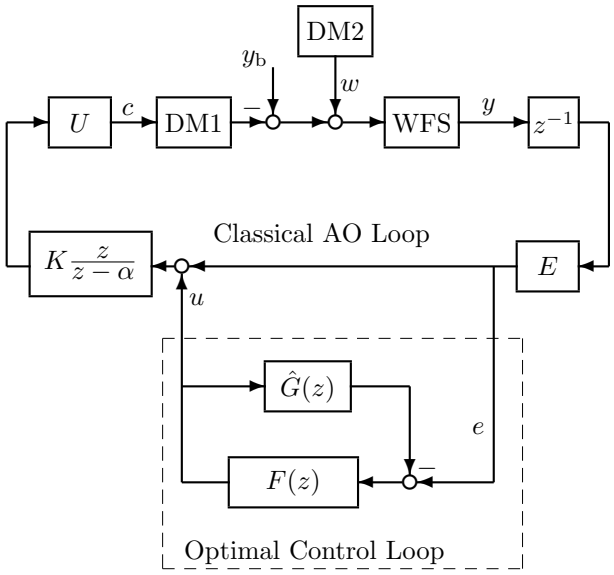

Figure 3. Block diagram of AO experiment with control loops.

B. Optimal Control

The optimal control loop is shown inside the dashed box in Figure 3. The optimal control loop augments the classical AO loop, which remains closed when the optimal control loop is closed. As shown in these block diagrams, the optimal controller is a feedback controller but its structure is based on a feedforward disturbance-rejection design with the optimal prediction filter $F(z)$, discussed in Section V.

For the optimal controller, the input is the wavefront error signal e and the output is the optimal control command u, both of which are in DM modal coordinates. The transfer function $\hat{G}(z)$ in Figure 3 is a model of the true transfer function $G(z)$ from u to e with only the classical AO loop closed. The optimal controller assumes that (4) and (5) hold, and this implies that $G(z)$ is a diagonal linear transfer function with each diagonal term given by

$$\hat{G}(z) = \frac{-K}{z + K - \alpha}. \tag{6}$$

In hardware applications, $G(z)$ and $\hat{G}(z)$ probably never are exactly equal, and often $G(z)$ is nonlinear.

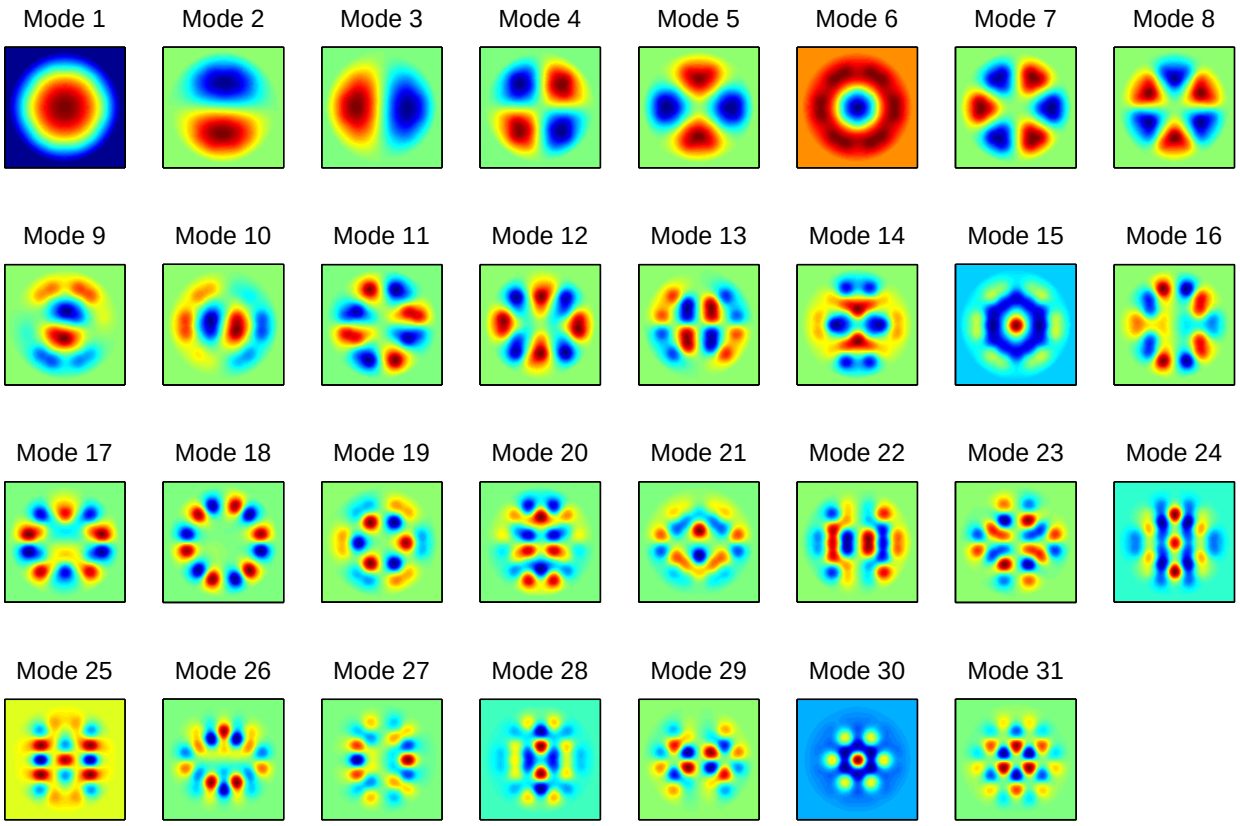

Figure 4. Deformable mirror modes.

V. Minimum-Variance Wavefront Prediction and System Identification

The one-step prediction filter has the state-space form

$$\begin{aligned} x(t+1) &= Ax(t) + K[y(t) - \hat{y}(t)] \\ \hat{y}(t) &= Cx(t) \end{aligned} \tag{7}$$

where $y(t)$ is a vectorized wavefront sequence, as represented by the modal coefficients, and t is the frame or sample number. The one-step prediction of $y(t)$ is $\hat{y}(t)$. The the relationship of the mathematical state vector $x(t)$ to the physics of the wavefront sequence is convoluted, so that the components of $x(t)$ (usually numbering in the hundreds) should be considered as just internal variables of the prediction model. The constant matrices A, C and K are identified by a subspace system identification method from a representative wavefront sequence. The multi-channel lattice-filter based subspace identification algorithm in 8 was used. The methods described here can be generalized to multi-step prediction. Most AO applications require either one or two-step prediction.

The statistics of the wavefront sequence are represented implicitly in the matrices A, C and K and the covariance matrix for the prediction-error or *innovations* sequence

$$e = y(t) - \hat{y}(t) \tag{8}$$

The one-step prediction model can be written in the innovations form

$$\begin{aligned} x(t+1) &= Ax(t) + Ke(t) \\ y(t) &= Cx(t) + e(t) \end{aligned} \tag{9}$$

Theoretically, with sufficiently long, stationary data sequences, the prediction error (i.e., the innovations sequence) is white, and the prediction filter becomes a steady-state Kalman filter. But the filter is not constructed in the classical way from a known plant model and assumed disturbance statistics, neither of which is known or assumed here.

For the experimental results in this paper, a 7000 frames of the experimentally measured aero-optical data were mapped to the DM2 geometry. The first 5000 frames were used to identify the A, C and K in (7). The remaining 2000 frames were used for the disturbance sequence in the experiment.

VI. Experimental Results

A. Performance Enhancements with Optimal Control

Figures 5 through 8 and Table 1 depict experimental results from applying turbulent wavefronts to the setup in Figure 2. A sequence of 7000 disturbance commands for DM2 were generated from the Notre Dame data. The first 5000 frames were used for identification of an optimal LTI controller, while the remaining 2000 were used in the experiment to compare controller performance.

Three control schemes were implemented. No correction was applied to the wavefront during the open-loop experiment, while only the classical AO loop shown in Figure 3 was closed for the integrator experiment. For the third experiment, an optimal LTI controller was first identified using the 5000 frame disturbance sequence with the classical AO loop closed. Then, the 2000 frame sequence was applied with the optimal LTI loop augmenting the classical loop as in Figure 3.

Figure 6 shows a portion of the RMS wavefront error time series for each of these experiments. While the classical AO loop addresses some of the open-loop error, the optimal LTI predictor further reduced the error at the majority of time steps. Table 1 summarizes the RMS wavefront error over time and space; while the classical AO loop reduced the open-loop RMS error by 22.5%, using the optimal controller resulted in a 46.5% reduction.

Mitigating the wavefront error resulted in an improvement in the maximum target intensity. Figure 5 shows the mean target intensity over 2000 frames for each experiment, where the wavefront error reduction with the optimal controller produced a significant increase in the peak average intensity compared to the classical controller. Part of this improvement can be attributed to the reduced movement in the peak location; shown in Table 1, the standard deviation of location of the maximum intensity dropped when the optimal controller was used. However at many samples the maximum value itself increased, as seen in the time series of the maximum intensity in Figure 6.

B. Modal Analysis

Further performance results can be seen by projecting the residual wavefronts from the experiments onto the DM modes in Figure 4, resulting in a time series of modal coefficients for each experiment. Figure 7 shows the power of the measured wavefronts in each mode (i.e. the temporal RMS of each modal sequence), and also the modal power for the classical and optimal cases normalized by the open-loop power. 15 of the 31 modes were used for control in both the classical and optimal loops, evidenced by the increase in the modal power in modes 16 through 31, relative to the open-loop case.

Figure 8 shows the power spectral densities for several representative modal sequences. The classical AO controller succeeds in reducing disturbances until approximately 1.5-2 kHz. However the optimal controller is effective for a considerably wider range of frequencies, showing significant improvement until 4 kHz in some modes.

Acknowledgments

Jon Tesch and Steve Gibson were supported by the High Energy Laser Joint Technology Office (HEL JTO) and the U.S. Office of Naval Research, ONR Grant number N00014 07-1-1063. Stanislav Gordeyev and Eric Jumperwere supported by the High Energy Laser Joint Technology Office (HEL JTO) and the U.S. Air Force Office of Scientific Research, AFOSR Grant number FA9550-07-1-0574.

Table 1. Performance measures for correction of wavefront error and improvement of on-target energy distribution.

Control Type	Wavefront error RMS (μm) over time and space	Peak intensity of average target image	Standard deviation of peak intensity position	
			horizontal	vertical
Open Loop	0.66	9.07	13.82	9.04
Classical AO Loop	0.51	16.53	9.97	5.31
Optimal Control	0.35	21.66	7.84	3.72

References

[1]J. S. Gibson, C.-C. Chang, and B. L. Ellerbroek, "Adaptive optics: wavefront correction by use of adaptive filtering and control," Applied Optics, Optical Technology and Biomedical Optics **39**, 2525–2538 (2000).

[2]Y.-T. Liu and J. S. Gibson, "Adaptive optics with adaptive filtering and control," in American Control Conference, (Boston, MA, 2004), pp. 3176–3179.

[3]T. A. Rhoadarmer, L. M. Klein, J. S. Gibson, N. Chen, and Y.-T. Liu, "Adaptive control and filtering for closed-loop adaptive-optical wavefront reconstruction," in SPIE Conference on Advanced Wavefront Control, vol. 6306, (SPIE, San Diego, CA, 2006), pp. 63060E–1–63060E–12.

[4]J. S. Gibson and Yu-tai Liu, "Adaptive control in adaptive optics for directed energy systems," Optical Engineering **46**, 046601–1–046601–13 (2007).

[5]Salman Monirabbasi and J. S. Gibson, "Adaptive control in an adaptive optics experiment with simulated turbulence-induced optical wavefronts," (SPIE, San Diego, CA, 2009), vol. 7466 of *SPIE Conference on Advanced Wavefront Control*, pp. 746608–1–746608–11.

[6]Salman Monirabbasi and Steve Gibson, "Adaptive control in an adaptive optics experiment," J. Opt. Soc. Am. A **27**, 84–96 (2010).

[7]C. Porter, S. Gordeyev, M. Zenk and E. Jumper, "Flight Measurements of Aero-Optical Distortions from a Flat-Windowed Turret on the Airborne Aero-Optics Laboratory (AAOL)," in 42nd AIAA Plasmadynamics and Lasers Conference, Honolulu, HI, June 2011.

[8]N. Chen and J. S. Gibson, "Subspace system identifcation using a multichannel lattice filter," in American Control Conference, (Boston, MA, 2004), pp. 855–860.

[9]C. Petit, J.-M. Conan, C. Kulcsár, H.-F. Raynaud, T. Fusco, J. Montri, F. Chemla, and D. Rabaud, "Off-axis adaptive optics with optimal control: Experimental and numerical validation," (2005), vol. 5903 of *Proc. SPIE*, pp. 227–235.

[10]K. Hinnen, M. Verhaegen, and N. Doelman, "Exploiting the spatio-temporal correlation in adaptive optics using data-driven H_2-optimal control," J. Opt. Soc. Am. A **24**, 1714–1725 (2007).

[11]C. Petit, J.-M. Conan, and C. Kulcsár, "LQG control for AO and MCAO: experimental and numerical analysis," J. Opt. Soc. Am. A **26**, 1307–1325 (2009).

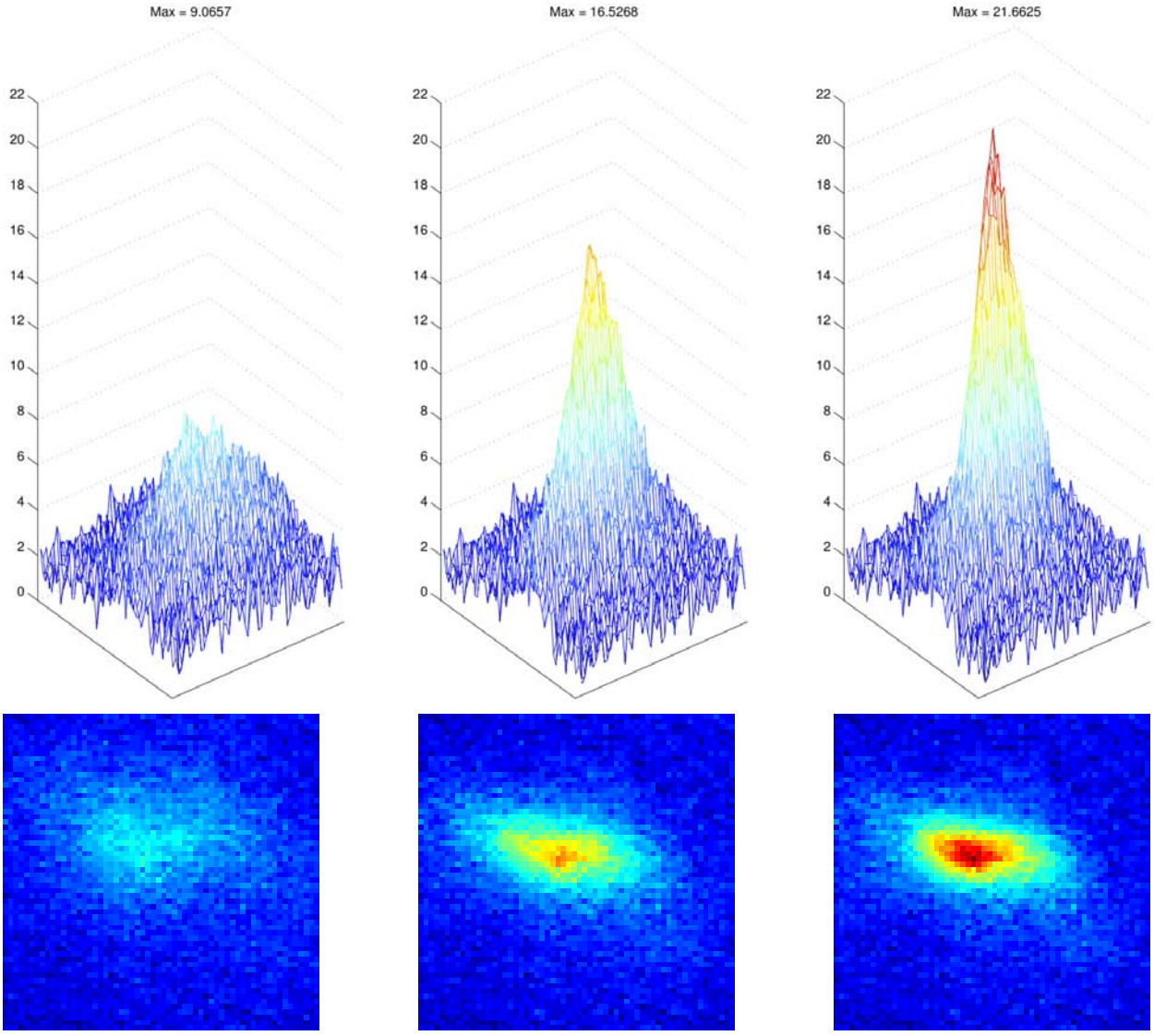

Figure 5. Average target camera images.

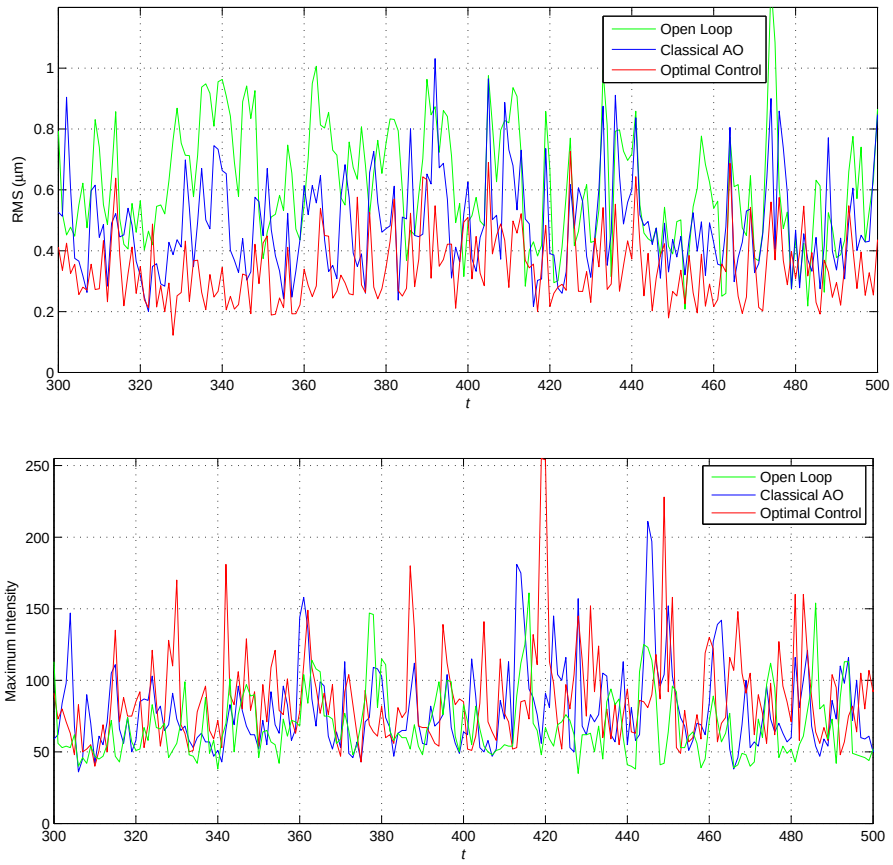

Figure 6. RMS and peak.

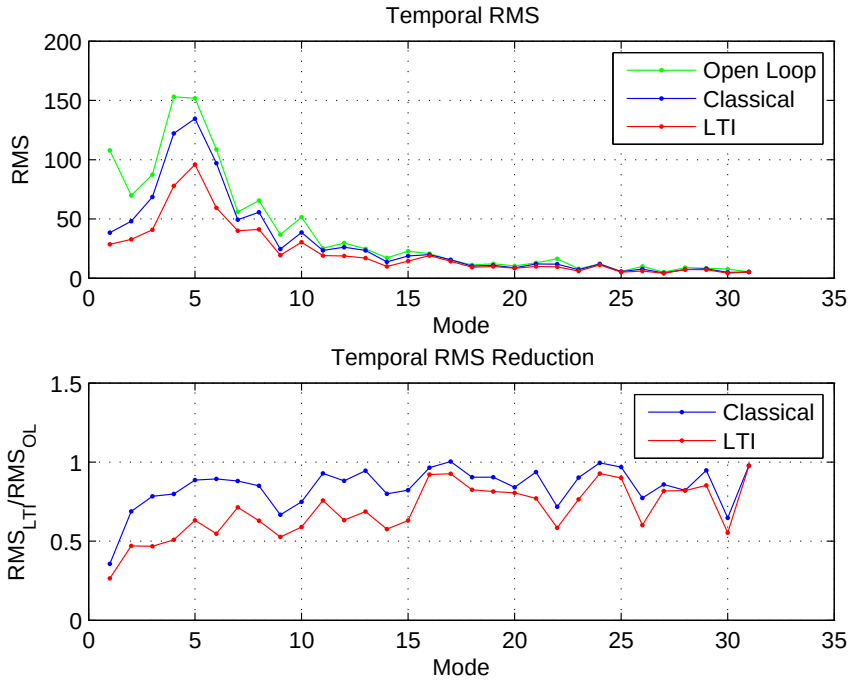

Figure 7. Modal power.

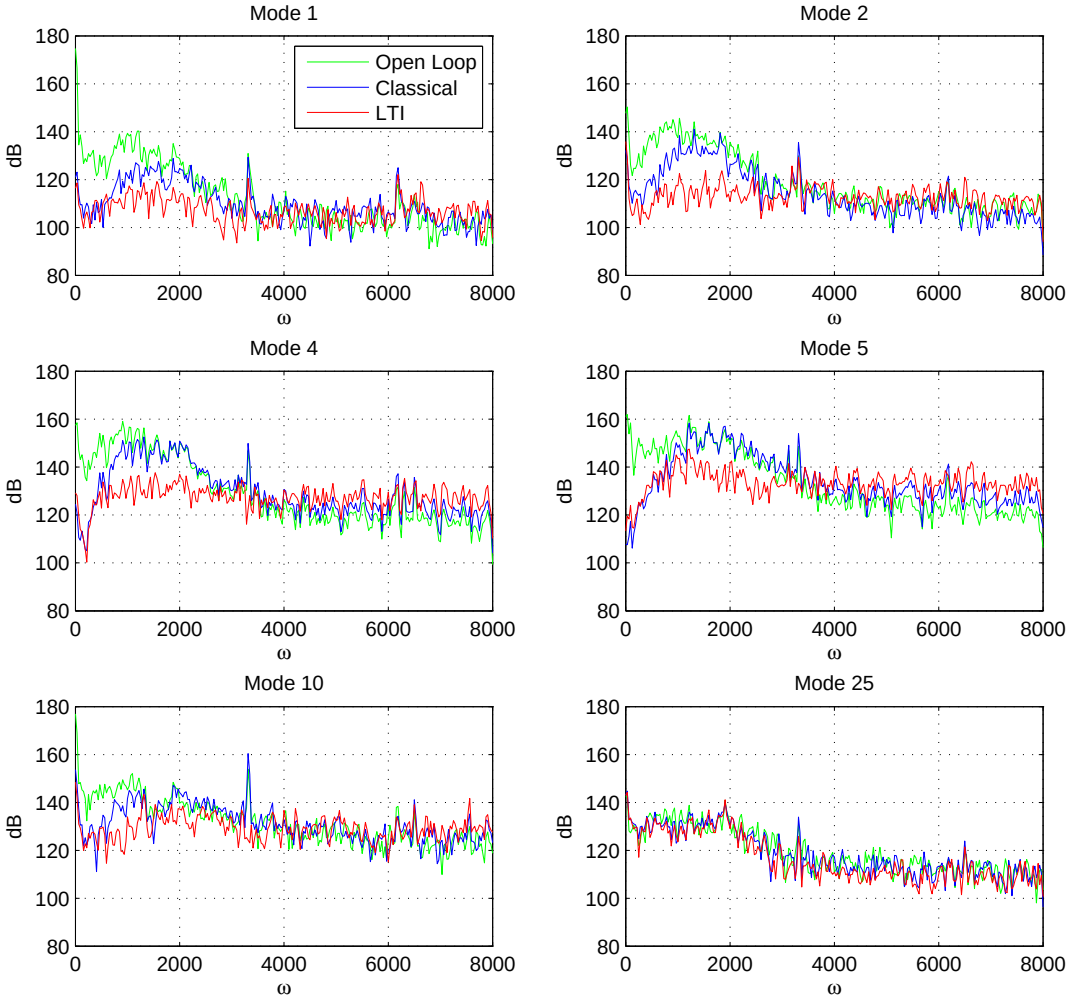

Figure 8. Power spectral densities of representative modal sequences.